Geophysical Research Letters

RESEARCH LETTER
10.1029/2025GL115935

Transient Darkening of Low-Level Liquid Clouds by the 2022 Hunga Lamb Wave Observed in GOES-R Imagery

Ákos Horváth[1], **David K. Adams**[2], **Mengqi Liu**[1,3], **Ignacio Sepúlveda**[4], **Mirjana Sakradzija**[5], **and Stefan A. Buehler**[1]

[1]Meteorological Institute, University of Hamburg, Hamburg, Germany, [2]El Instituto de Ciencias de la Atmósfera y Cambio Climático, Universidad Nacional Autónoma de México, Mexico City, Mexico, [3]Key Laboratory of Atmospheric Sounding, Chengdu University of Information Technology, Chengdu, China, [4]Department of Civil, Construction and Environmental Engineering, San Diego State University, San Diego, CA, USA, [5]Department of Geography, Ludwig-Maximilians Universität, München, Germany

Abstract The 15 January 2022 eruption of the Hunga volcano generated a Lamb wave, a global atmospheric pressure perturbation which propagates purely horizontally at the speed of sound. Far-field observations of the daytime passage of the Lamb wave by the Geostationary Operational Environmental Satellite-R (GOES-R) series, revealed unexpected, synchronized variations in the solar reflectance of low-level liquid clouds, the most prominent of which is a transient darkening accompanying the overpressure peak. We hypothesize that this darkening is mostly caused by the rapid thermodynamic adjustment of the cloudy environment to the slight, but spatially coherent, warming introduced by the pressure pulse. The corresponding reduction in relative humidity leads to the shrinkage and evaporation of small cloud droplets and hygroscopic particles in the halo region, which, in turn, temporarily reduces the optical thickness of the cloudy column.

Plain Language Summary The giant Hunga volcano explosion on 15 January 2022 produced a special atmospheric wave, called the Lamb wave, that traveled around the globe somewhat faster than a jetliner. The Lamb wave increased the atmospheric pressure, slightly warming the air. Geostationary time loop imagery recorded the movement of this wave over the Gulf of Mexico, the Caribbean, and the North Atlantic Ocean during daytime hours. The observations reveal that the passing Lamb wave turned low-level clouds momentarily darker. We argue that the cloud darkening is caused by the shrinkage of droplets inside and near clouds due to the warming.

Key Points:

- The Hunga Lamb wave caused detectable brightness variations in low-level clouds 12,000 km away
- The dominant signal is a temporary darkening accompanying the peak overpressure
- We hypothesize the darkening results from the shrinkage of drops due to a sudden increase in temperature and decrease in relative humidity

Supporting Information:

Supporting Information may be found in the online version of this article.

Correspondence to:

Á. Horváth,
hfakos@gmail.com

Citation:

Horváth, Á., Adams, D. K., Liu, M., Sepúlveda, I., Sakradzija, M., & Buehler, S. A. (2025). Transient darkening of low-level liquid clouds by the 2022 Hunga Lamb wave observed in GOES-R imagery. *Geophysical Research Letters*, *52*, e2025GL115935. https://doi.org/10.1029/2025GL115935

Received 13 MAR 2025
Accepted 12 JUN 2025

Author Contributions:

Conceptualization: Ákos Horváth
Data curation: David K. Adams
Formal analysis: Ákos Horváth, David K. Adams, Mengqi Liu, Ignacio Sepúlveda, Mirjana Sakradzija, Stefan A. Buehler
Funding acquisition: Ákos Horváth
Investigation: Ákos Horváth, David K. Adams, Mengqi Liu, Ignacio Sepúlveda, Mirjana Sakradzija, Stefan A. Buehler
Methodology: Ákos Horváth
Project administration: Ákos Horváth
Software: Ákos Horváth
Visualization: Ákos Horváth
Writing – original draft: Ákos Horváth
Writing – review & editing: David K. Adams, Mengqi Liu,

1. Introduction

The eruption of the Hunga submarine volcano on 15 January 2022 was a record-setting explosion in many aspects. It produced the tallest eruption column of ~57 km (Carr et al., 2022), the most intense lightning activity (Bór et al., 2023; Van Eaton et al., 2023), the highest volumetric flow rate (Prata et al., 2025), and the largest stratospheric water vapor injection (Khaykin et al., 2022; Millán et al., 2022; Randel et al., 2023) ever measured. A wide spectrum of atmospheric waves was generated, including gravity waves (GWs) and acoustic waves (Horváth et al., 2024; Matoza et al., 2022; Vergoz et al., 2022; Wright et al., 2022), and a never-before-observed global resonant mode called the Pekeris wave (Pekeris, 1937; Watanabe et al., 2022). The atmospheric pressure wave excited fast-moving meteotsunamis (Kubota et al., 2022; Purkis et al., 2023), while secondary GWs created by the breaking of the primary GWs induced traveling ionospheric disturbances (Vadas et al., 2023).

Although Hunga's climate impact is likely to be modest (Sicard et al., 2025; Stocker et al., 2024; Wang & Huang, 2024), the triggered planetary-scale disturbances provide a singular opportunity to advance our understanding of a variety of geophysical processes. The most prominent disturbances were the multiple passages of a Lamb wave, a special acoustic wave whose vertically uniform phase fronts propagate purely horizontally leading to surface pressure perturbations as well as strong signals in geostationary satellite imagery around the globe. These observations have been employed to improve a Lamb wave model for meteotsunami prediction, including the crucial steering effects of global winds and topography (Sepulveda et al., 2023). As noted above, the numerous prior studies have concentrated on surface or upper-atmospheric wave effects. In this study, a rather unexpected phenomenon allows us to examine Lamb wave-induced cloud modifications in various channels of satellite imagery.

Ignacio Sepúlveda, Mirjana Sakradzija, Stefan A. Buehler

The pressure waveform changed with each Lamb wave passage. During the first, and strongest, passage, the leading overpressure was the salient feature in far-field records. The sharp compression peak dropped in 10–15 min to a smaller negative rarefaction trough, followed by a longer equalization phase. The compression and rarefaction caused in-phase warming and cooling temperature anomalies, detectable in thermal infrared (IR) satellite data (Horváth et al., 2024; Otsuka, 2022; Watada et al., 2023). Previous studies analyzed emissive IR channels exclusively, permitting day-and-nighttime Lamb wave tracking (e.g., Wright et al., 2022). In contrast, here we focus on Lamb wave effects on solar reflectance channels, including visible wavelengths. The Geostationary Operational Environmental Satellite-16 (GOES-16) Continental US (CONUS) scan captured the first wave passage during nighttime in the western section and during daytime in the eastern section of the domain. Remarkably, the Lamb overpressure caused a transient decrease in reflectance in low-level liquid clouds ∼12,000 km from Hunga. This darkening, we hypothesize, reflects the nearly instantaneous adjustment of the cloudy environment to a slight, but spatially coherent, reduction in relative humidity accompanying the Lamb wave warming, discernible as a momentary dimming of cloudy regions.

The fundamental role that marine liquid clouds play in the Earth's climate, particularly their role in modulating reflected solar radiation, has been a central issue in climate change and aerosol-cloud microphysics interactions (Bellouin et al., 2020; Goessling et al., 2025). Many observational and modeling studies have focused on marine cloud adjustments to increased aerosol or CO_2 concentrations on timescales of hours to days (Andrews et al., 2012; Zhou et al., 2025). With the Lamb wave, we have a unique opportunity to specifically challenge models to reproduce cloud reflectance adjustments to these extremely fast pressure perturbations, and to ascertain the validity of model parameterizations and representation of relevant liquid cloud microphysics as well as to confirm or refute our hypothesis.

2. Pressure and Temperature Signature of the First Lamb Wave Passage

The magnitude and shape of published Hunga pressure anomalies do vary somewhat; nevertheless, the far-field waveforms are quite similar. Figure 1 insets show two pressure anomaly records typical over the southern portion of CONUS. The TLALOCNet (Trans-boundary, Land and Atmosphere Long-term Observational and Collaborative Network; Cabral-Cano et al., 2018) station in La Concepción, Jalisco, Mexico (TNLC, 1-min sampling) is in the domain's western part ∼8,899 km from Hunga, while PurpleAir station 7518 at the University of The Bahamas in Nassau (UofB, 2-min sampling) is in the eastern part ∼11,732 km from Hunga. They represent a nighttime (12:18 UTC) and daytime (14:43 UTC) Lamb wave arrival, respectively.

The full wave packet envelope has a 30–40 min period. The eruption sequence between 04:15 and 04:30 UTC that produced the main Lamb pulse included two smaller preceding pulses (Horváth et al., 2024; Matoza et al., 2022). The maximum overpressure at TNLC and UofB was 2.1 and 2.6 hPa, respectively. The pressure anomaly then dropped to smaller troughs of −0.5 and −0.7 hPa in about 10–14 min, during a longer and more fluctuating negative phase. Watada et al. (2023) found similar compression–rarefaction asymmetry in Japanese pressure records (+1.6 hPa overpressure, −0.5 hPa trough). Such asymmetry between the positive and negative pressure phases is characteristic of controlled atmospheric explosions. Infrasound propagation experiments of typical blast-waves reveal firstly the overpressure peak, then a smaller negative pressure trough behind the shock front followed by a relatively long equalization phase (Fee et al., 2013). The positive phase amplitude and duration can be twice as large and half as long as those of the negative phase (Bonner et al., 2013).

Similarly, the Lamb wave's dominant perturbation is a sudden surface overpressure of 2–3 hPa within a positive anomaly phase of 10–15 min duration. Assuming adiabatic compression and a perturbation that exponentially decreases with altitude (Garrett, 1969; Watada et al., 2023; Text S1 in Supporting Information S1), such an overpressure yields a temperature increase of 0.2–0.3 K in the boundary layer (up to ∼2 km altitude). The subsequent temperature decrease during the rarefaction phase is a significantly smaller and more gradual anomaly.

3. Visualizing the Lamb Wave in GOES-16 Imagery

We utilized reflectance factor (R, henceforth “reflectance”) from the daytime reflective channels C1–C6 and brightness temperature (BT) from the day-night emissive channels C7–C16 of the Advanced Baseline Imager (ABI), available at 5-min cadence over the CONUS. All channels were mapped to a common 2-km resolution. For a detailed description of the ABI spectral bands, the reader is referred to Schmit et al. (2017, 2018).

10.1029/2025GL115935

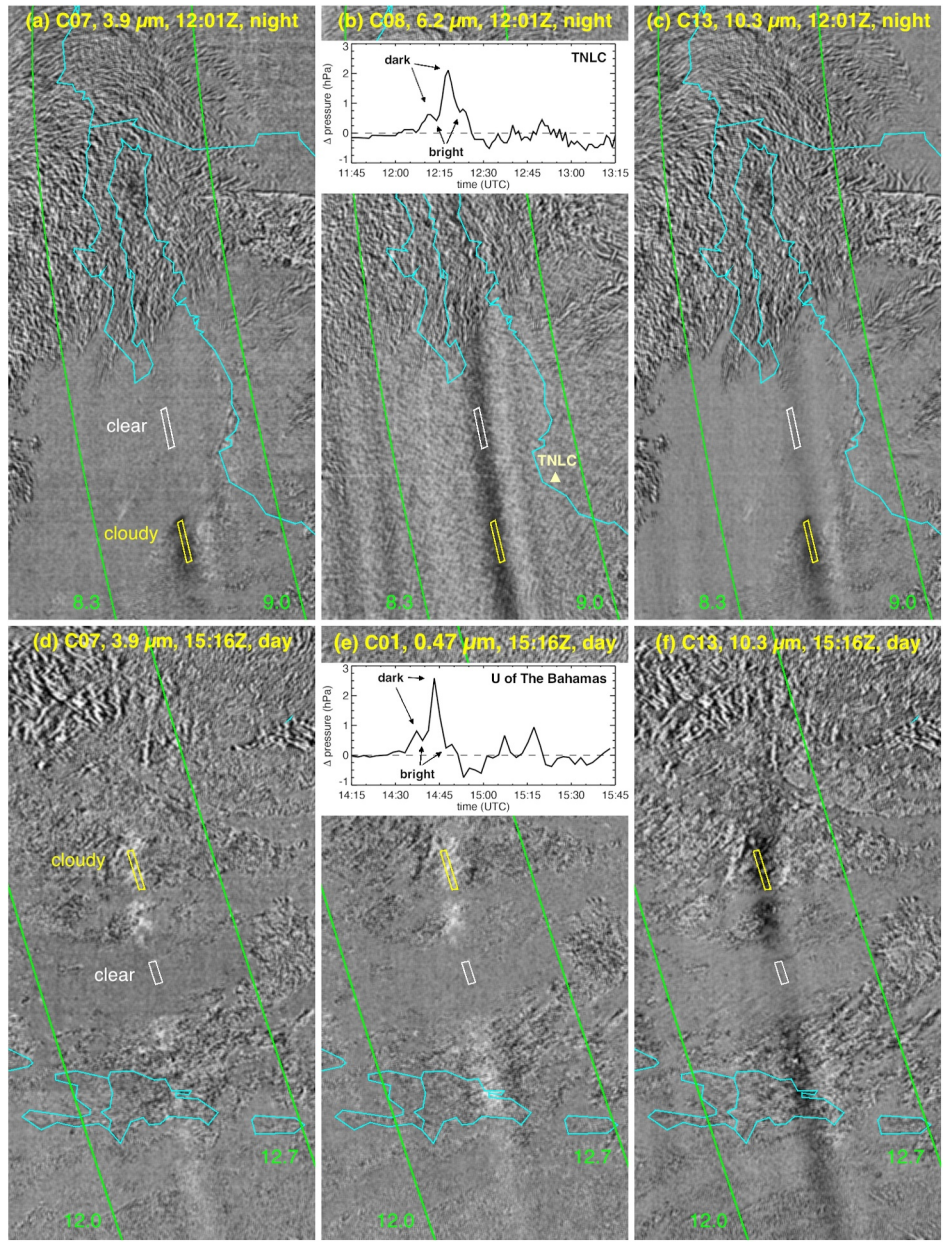

Figure 1. Second time derivative of GOES-16 brightness temperature and reflectance for a nighttime (12:01 UTC, top row) and daytime (15:16 UTC, bottom row) area in the CONUS sector on 15 January 2022. The selected channels are (a) C7, (b) C8, and (c) C13 for night and (d) C7, (e) C1, and (f) C13 for day. White and black shades correspond to positive and negative second derivatives, respectively. The insets show the surface pressure anomaly relative to a 2-hr moving average at the nearest night station of TNLC (beige triangle) and day station at the University of The Bahamas (out and west of the frame). The Lamb wave's overpressure peak is depicted by the thick black or white stripe. The analyzed clear and cloudy domains are marked by white and yellow, respectively. The green lines are isodistances (×1,000 km) from Hunga.

Of the reflective channels, bands 1 and 2 are the visible blue and red bands, while bands 3–6 are near-IR bands. Bands 3, 5, and 6 are used together with the red band to retrieve cloud drop size and optical thickness. Band 4 senses thin cirrus or contrails due to strong absorption by water vapor (WV). Of the emissive channels, band 7 needs special mention, being a hybrid band sensitive to both terrestrial IR radiation and reflected solar radiation during daytime. Bands 8, 9, and 10 are the upper-, mid-, and lower-level WV channels, whose weighting function peaks at ∼8, ∼6, and ∼4 km, respectively. Band 12, the "ozone" band, has a weighting function that peaks the highest at ∼22 km. Finally, bands 11 and 13–16 are IR window channels with varying degrees of "dirtiness," that

is, sensitivity to WV and trace gas absorption. For interpreting our results, the most relevant point is that apart from the three WV bands, all other IR bands are generally sensitive to low-level clouds and the planetary surface.

We visualize the Lamb wave by taking the second time derivative of BT and R (denoted by BT″ and R″). The time derivative images are gray scaled, spatially smoothed with a boxcar filter, and histogram equalized to increase visual contrast (Horváth et al., 2024). Employing the time derivative greatly diminishes the heterogeneous background comprising clear and cloudy patches and enhances the spatially coherent signal from the fast-propagating waves. In the resulting images, the main Lamb pulse appears as an ∼80 km wide dark or bright stripe. Blackish shades generally correspond to negative second derivatives or local maxima in BT or R, and whiteish shades refer to positive second derivatives or local minima in BT or R (the maxima and minima were also confirmed by a first-derivative test).

4. Radiometric Signature: Warming in Emissive Bands and Darkening in Reflective Bands

Figure 1 shows nighttime (12:01 UTC, top row) and daytime (15:16 UTC, bottom row) snapshots of the Lamb wave in four selected channels. Time loops for these channels and snapshots for all 16 channels are given in Supporting Information S1. Note that the wave moves ∼100 km between consecutive images. During nighttime, the main Lamb pulse causes warming in all emissive channels (negative BT″, black stripe). The same holds true during daytime, except for the hybrid C7 which displays cooling anomalies (positive BT″, white stripe). Movie S3 depicts how the C7 Lamb signature transitions from warming to cooling as the wave traverses the CONUS west-to-east and the reflected component contribution increases after sunrise. Similarly, the Lamb pulse introduces a negative, or darkening, anomaly in all purely reflective channels.

The higher altitude-sensing WV and ozone channel time derivatives are strongest and more uniform. In the more surface-sensing IR window channels, however, the signal is much weaker in clear areas than in cloudy regions: the smaller the WV or trace gas absorption, the weaker the signal in cloud-free areas. Thus, the clear–cloudy contrast is the largest in C13 (“clean” window) and smallest in C15 (“dirty” window). Furthermore, there is no reflectance signal in clear areas. These results highlight that the Lamb wave's perturbation is overwhelmingly contained in the atmosphere, moving too fast to leave a detectable signal in surface temperature or reflectance.

For quantitative analysis, we selected clear and cloudy marine domains within the nighttime and daytime Lamb stripes, as marked in Figure 1. The cloudy domains are not overcast and include clear gaps between clouds. The night cloudy domain contains thin stratus and small cumuli with tops near ∼500 m, as retrieved by the Level 2 cloud height product (GOES R, 2020a). The daytime cloudy domain contains thicker liquid clouds with maximum heights at ∼2 km. Cloudy scene images are given in Figure S4 in Supporting Information S1. The Lamb anomaly was extracted by removing the 35-min moving average from the domain-mean BT or R time series (the unfiltered cloudy data are plotted in Figure S5 in Supporting Information S1).

As shown in Figure 2, the dominant BT anomaly is a warming in the compression phase, followed by a smaller cooling in the weaker rarefaction phase. In the clear domains, the warming ranges between 0.02 and 0.11 K, the signal being strongest in the WV channels. In the window channels, the positive anomaly is considerably smaller but tends to increase with the “dirtiness” of the band. Solar reflectance, however, does not show a detectable anomaly in the clear domains.

Regarding the Lamb signal in the cloudy domains, we note three salient points. One, the apparent BT warming is several times larger than in clear areas, ranging from 0.11 K up to 1.30 K. The increase is especially large in the window channels, while in the higher altitude WV channels the anomaly only rises from ∼0.1 to ∼0.2 K. Two, the warming is much larger in the daytime versus nighttime domain. Three, all reflectance channels exhibit darkening and the hybrid C7 flips from warming to cooling. Depending on the channel, the domain-mean reflectance decreases by 9%–14% during the passage of the Lamb wave.

These observations suggest that the cloudy domain Lamb signal is modulated by the changing properties of low-level clouds, which regulate the surface contribution. Thus, the actual warming of 0.2–0.3 K gets amplified in the domain-mean BT. The domain-mean brightness temperature and reflectance are weighted averages of warm and dark surface pixels and cold and bright cloud pixels. If the temperature increase caused by the Lamb overpressure reduces the opacity or area fraction of low-level clouds, the contribution from the warm and dark surface increases in the mean, leading to an amplified warming and darkening signal. The amplification depends on the magnitude

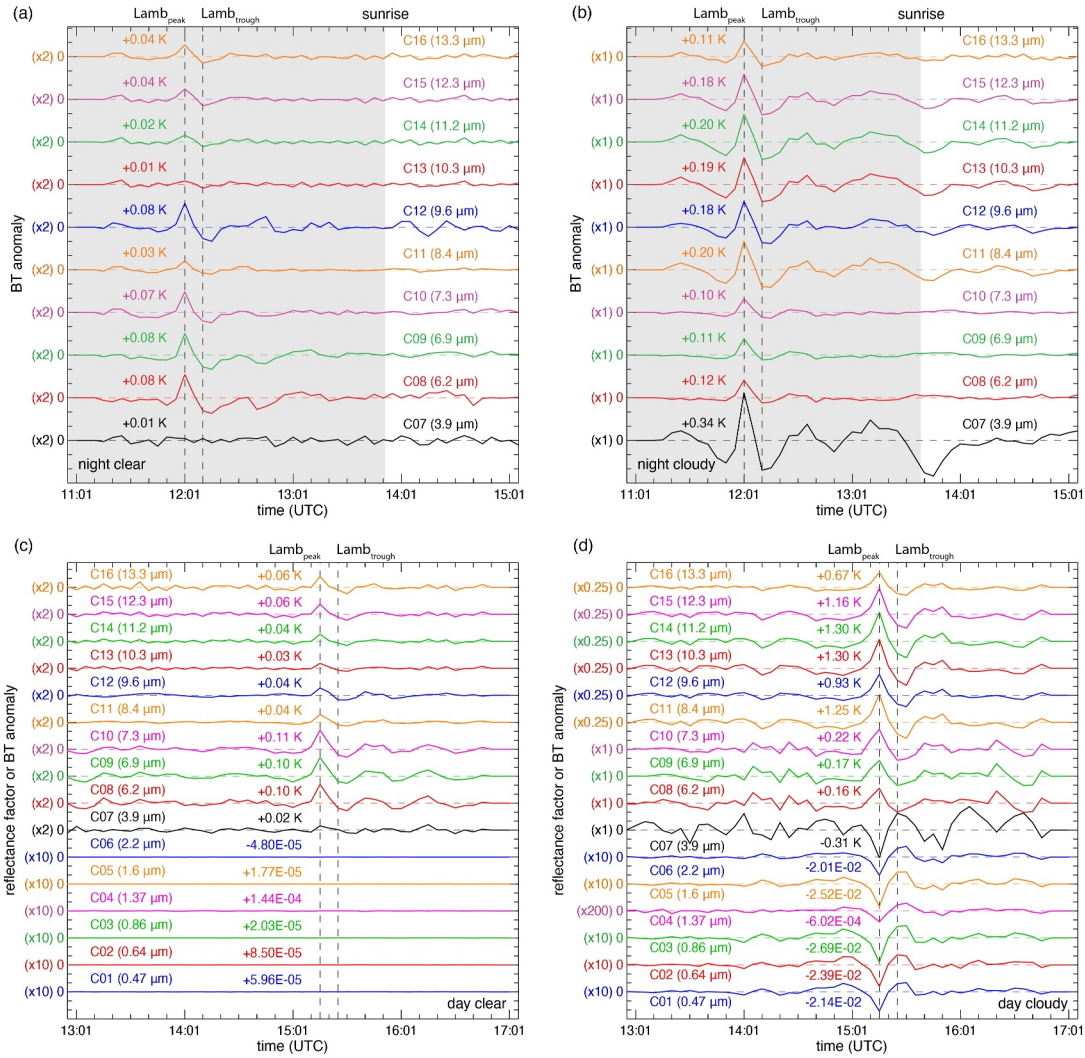

Figure 2. Mean brightness temperature and reflectance anomalies over a 4-hr period for the (a) night clear, (b) night cloudy, (c) day clear, and (d) day cloudy domains in Figure 1. In panels (a) and (b), gray shading indicates nighttime. The horizontal dashed lines mark the zero (0) line for each stacked anomaly curve. A tick mark is 0.1 unit (K or sr^{-1}) and the channel-dependent plotting scale factor is given in parenthesis. The arrival times of the Lamb wave's peak and trough are marked by the vertical dashed lines. The actual (unscaled) BT and R anomalies at the arrival of the Lamb overpressure are also indicated.

of the temperature and reflectance contrast between the surface and the clouds in a given band. For example, the band 13 surface–cloud BT contrast is 18 K in the daytime domain but only 5 K in the nighttime domain, because the cloud tops are higher and colder in the former than in the latter (~2 km, ~275 K vs. ~500 m, ~290 K), while the ocean BT is 293–295 K in both. This explains the larger apparent warming signal in the daytime cloud domain. The low-level cloud darkening is not readily perceivable in static reflectance images; however, it is faintly discernible when the raw images are animated, as shown by Movies S6 and S7.

The decrease in reflectance is large enough to affect the retrieval of cloud optical depth (COD) and cloud drop effective radius (CER). The daytime algorithm is a bi-spectral method that combines the visible red C2 with one of the near-infrared C3, C5, or C6; the default being C6 (GOES R, 2020b). Reflectance in these channels is interpreted assuming a single-layered, plane-parallel, homogeneous cloud that completely covers a pixel. Reflectance in C2 increases primarily due to an increase in COD, while reflectance in C6 increases mostly due to a decrease in CER.

In this 1D retrieval framework, a simultaneous darkening of C2 and C6 leads to a smaller COD and a larger CER, as depicted in Figure 3. Here, we used the median to characterize the shift in the distribution of the retrieved cloud

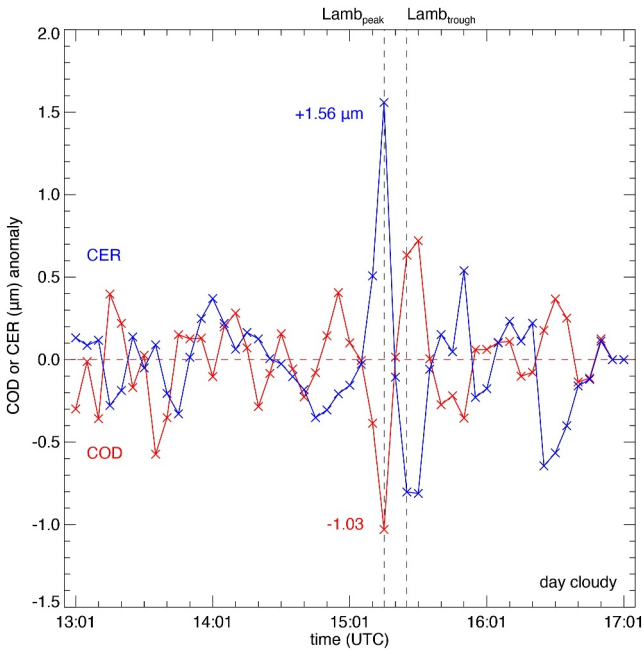

Figure 3. Median cloud optical depth and cloud drop effective radius anomalies over a 4-hr period for the day cloudy domain.

properties. The mapping between reflectances and COD and CER is affected by the saturation of C2 for large COD and by the high uncertainty of CER in thin, broken clouds. The median filter reduces the noise arising from the occasional retrieval of unphysically large COD or CER values. Whether the CER increase is real, or it is a retrieval artifact due to neglected 3D radiative effects, needs to be resolved by further research.

The COD and CER anomalies fluctuate within ±0.5 and are essentially uncorrelated before the Lamb wave's arrival (correlation coefficient −0.28). During the passage of the overpressure peak, the median COD drops by ∼1.0 and the CER jumps by ∼1.6 µm. Opposite, but smaller anomalies occur 10–15 min later as the wave trough passes and causes a slight brightening. The COD and CER anomalies become highly anti-correlated after the Lamb wave's arrival (correlation coefficient −0.91), indicating the presence of darkening–brightening fluctuations of diminishing amplitude in the wake of the main pulse.

5. Potential Cause of Cloud Darkening

Gravity wave-induced BT variations were previously noted in upper-level moisture layers and marine stratocumulus decks, interpreted as humidity or cloud-top height undulations caused by vertical oscillations (Allen et al., 2013; Connolly et al., 2013; Vicari et al., 2024). As the cloud is periodically lifted and lowered, it thickens and cools and then warms and dissipates, with additional entrainment of warm, dry air from above the inversion boosting cloud thinning. The observed GWs, however, had low phase velocities (∼15 m s^{-1}) and long periods (∼1.5 hr), which allowed adjustment processes considerable time to modulate cloud properties. In contrast, the Lamb wave moves at the speed of sound (∼20 times faster) and supports purely horizontal pressure and temperature fluctuations without vertical oscillations (Bretherton, 1969). This points to rapid and mostly thermodynamic adjustments, we argue, that act within minutes.

The darkening is of similar magnitude in visible and near-infrared bands, which rules out strongly wavelength-dependent effects such as perturbations in Rayleigh scattering or trace gas absorption. The reflectance reduction is most apparent in low-level clouds, both over land and ocean (see animations in Supporting Information S1). These liquid clouds are surrounded by a transition zone, where the thermodynamic and radiative properties of the cloudy atmosphere gradually transition into those of clear sky. Compared to clear sky, the transition zone is characterized by enhanced humidity, turbulence, and particle formation (Perry & Hobbs, 1996), which in turn leads to enhanced near-cloud reflectance due mainly to hygroscopic particle growth (Koren et al., 2007; Mieslinger et al., 2022; Tackett & Di Girolamo, 2009; Twohy et al., 2009; Várnai & Marshak, 2009). The particle size and scattering enhancements are ubiquitous over all oceans and are strongest slightly below cloud top (Várnai & Marshak, 2011).

The droplet size distribution in the transition zone is governed by a complex web of entrainment, mixing, and evaporation processes. The various mixing and evaporation timescales, such as the single droplet evaporation timescale, droplet population phase relaxation timescale, and saturation restoration timescale, all vary between 2 and 20 s (Tölle & Krueger, 2014) and, thus, allow the rapid adjustment of the transition zone to a fast-propagating perturbation. In situ measurements and Mie calculations show that the scattering cross-section of hygroscopic particles increases very sharply with RH when RH > 90%–95% (Hess et al., 1998; Su et al., 2008). Marine aerosols containing sea salt generally exhibit the largest enhancements. Airborne observations of trade cumulus in the Indian Ocean by Twohy et al. (2009) found a distinct rise in RH from ∼90% at 1 km from cloud edge to saturation at the cloud edge, with half the rise occurring within the last 100 m before the edge. Measurements with the Multichannel Cloud Radiometer (MCR) at 0.64 and 1.06 µm showed a 50%–70% upward reflectance enhancement corresponding to the 5%–10% RH increase in the transition zone. Similar to our findings, the MCR reflectance variations revealed no wavelength dependence either.

As discussed earlier, the Lamb overpressure of 2–3 hPa leads to a warming of 0.2–0.3 K in the boundary layer. A warming of such magnitude reduces RH by 1%–2% (Text S2 in Supporting Information S1). If we assume,

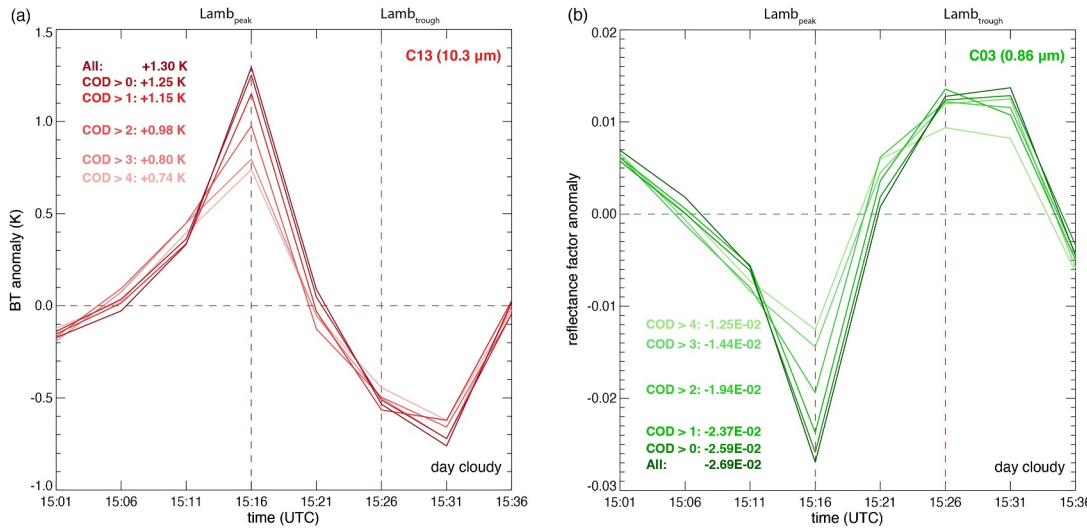

Figure 4. Zoom in on the cloud optical depth dependence of the mean (a) C13 BT anomaly and (b) C3 reflectance anomaly for the day cloudy domain during the Lamb wave's passage. The "All" case is the same as in Figure 2d, which includes all clear and cloudy pixels in the domain mean. The other cases restrict the averaging to progressively thicker and thicker parts of the clouds.

lacking more comprehensive in situ data, that the Twohy et al. (2009) measurements are broadly representative of marine clouds, a 1%–2% decrease in RH could plausibly cause a ∼10% decrease in reflectance, comparable to our findings. The adjustment of aerosol and cloud droplet size and radiative properties to the RH perturbation is presumed to be strongest near cloud edges. Figure 4 plots the C13 BT and C3 reflectance anomalies during the Lamb wave's passing as a function of COD. Consistent with expectations, the C13 warming and C3 darkening both steadily diminish as clear pixels and semi-transparent areas near cloud edges are excluded from the averaging. The magnitude of the anomalies gets halved when only the more opaque pixels in the cloud interiors with COD > 4 are considered.

6. Summary

The planetary-scale waves from the 2022 Hunga eruption provide a unique means to probe the atmosphere. In this vein, we analyzed far-field (CONUS) satellite observations of the Lamb pressure wave in the previously neglected solar reflectance bands, including visible wavelengths. Surprisingly, the Lamb wave triggered brightness variations in low-level clouds ∼12,000 km from the source, most notably a transient darkening accompanying the peak overpressure. We advance the admittedly speculative hypothesis that this darkening is caused by the adjustment of clouds and their transition zone to the small but spatially coherent adiabatic warming due to the Lamb wave. The shrinking of near-cloud hygroscopic aerosols and the evaporation of the smallest cloud droplets under a slightly decreased relative humidity can reduce the optical thickness and lead to the temporary dimming of the cloudy column. The lack of vertical oscillations in the Lamb wave, moving purely horizontally at the speed of sound, points to such rapid thermodynamic adjustments. Nevertheless, the contribution of dynamic adjustments cannot be ruled out completely. The pressure pulse also introduced a radial wind change of ∼0.5 m s^{-1} (Watada et al., 2023), which might have accelerated turbulent mixing and drying through the cloud sides. We believe this unexpected phenomenon represents an uncharted territory, whose detailed exploration will require the analysis of additional daytime satellite imagery of the wave throughout the world. Furthermore, imposing this Lamb wave horizontal pressure perturbation should be straightforward in large eddy simulations, and, therefore, the model microphysics, dynamics, and radiation schemes should replicate this observed darkening behavior and verify or reject our hypothesis.

Data Availability Statement

GOES-16 data sets are publicly accessible through Amazon Web Services (AWS, 2025). We acknowledge the use of imagery from NASA's Worldview application (https://worldview.earthdata.nasa.gov), part of NASA's

Earth Science Data and Information System (ESDIS). The TNLC and PurpleAir station 7518 pressure data are freely available at EarthScope (2025) and PurpleAir (2025).

Acknowledgments
Á.H. was supported by the Deutsche Forschungsgemeinschaft (DFG) as part of the Research Unit VolImpact, subproject VolPlume (FOR2820, DFG Grant 398006378). We acknowledge financial support from the Open Access funding enabled and organized by Projekt DEAL.

References

Allen, G., Vaughan, G., Toniazzo, T., Coe, H., Connolly, P., Yuter, S. E., et al. (2013). Gravity-wave-induced perturbations in marine stratocumulus. *Quarterly Journal of the Royal Meteorological Society*, *139*(670), 32–45. https://doi.org/10.1002/qj.1952

Andrews, T., Gregory, J. M., Forster, P. M., & Webb, M. J. (2012). Cloud adjustment and its role in CO_2 radiative forcing and climate sensitivity: A review. *Surveys in Geophysics*, *33*(3–4), 619–635. https://doi.org/10.1007/s10712-011-9152-0

AWS. (2025). Amazon Web Services (AWS) [Dataset]. Retrieved from https://registry.opendata.aws/noaa-goes/

Bellouin, N., Quaas, J., Gryspeerdt, E., Kinne, S., Stier, P., Watson-Parris, D., et al. (2020). Bounding global aerosol radiative forcing of climate change. *Reviews of Geophysics*, *58*(1), e2019RG000660. https://doi.org/10.1029/2019RG000660

Bonner, J., Waxler, R., Gitterman, Y., & Hofstetter, R. (2013). Seismo-acoustic energy partitioning at near-source and local distances from the 2011 Sayarim explosions in the Negev Desert, Israel. *Bulletin of the Seismological Society of America*, *103*(2A), 741–758. https://doi.org/10.1785/0120120181

Bór, J., Bozóki, T., Sátori, G., Williams, E., Behnke, S. A., Rycroft, M. J., et al. (2023). Responses of the AC/DC global electric circuit to volcanic electrical activity in the Hunga Tonga-Hunga Ha'apai eruption on 15 January 2022. *Journal of Geophysical Research: Atmospheres*, *128*(8), e2022JD038238. https://doi.org/10.1029/2022JD038238

Bretherton, F. P. (1969). Lamb waves in a nearly isothermal atmosphere. *Quarterly Journal of the Royal Meteorological Society*, *95*(406), 754–757. https://doi.org/10.1002/qj.49709540608

Cabral-Cano, E., Pérez-Campos, X., Márquez-Azúa, B., Sergeeva, M. A., Salazar-Tlaczani, L., DeMets, C., et al. (2018). TLALOCNet: A continuous GPS-Met backbone in Mexico for seismotectonic and atmospheric research. *Seismological Research Letters*, *89*(2A), 373–381. https://doi.org/10.1785/0220170190

Carr, J. L., Horváth, Á., Wu, D. L., & Friberg, M. D. (2022). Stereo plume height and motion retrievals for the record-setting Hunga Tonga-Hunga Ha'apai eruption of 15 January 2022. *Geophysical Research Letters*, *49*(9), e2022GL098131. https://doi.org/10.1029/2022GL098131

Connolly, P. J., Vaughan, G., Cook, P., Allen, G., Coe, H., Choularton, T. W., et al. (2013). Modelling the effects of gravity waves on stratocumulus clouds observed during VOCALS-UK. *Atmospheric Chemistry and Physics*, *13*(14), 7133–7152. https://doi.org/10.5194/acp-13-7133-2013

EarthScope. (2025). EarthScope Consortium [Dataset]. Retrieved from https://gage-data.earthscope.org/archive/met/2022/015

Fee, D., Waxler, R., Assink, J., Gitterman, Y., Given, J., Coyne, J., et al. (2013). Overview of the 2009 and 2011 Sayarim infrasound calibration experiments. *Journal of Geophysical Research: Atmospheres*, *118*(12), 6122–6143. https://doi.org/10.1002/jgrd.50398

Garrett, C. J. R. (1969). Atmospheric edge waves. *Quarterly Journal of the Royal Meteorological Society*, *95*(406), 731–753. https://doi.org/10.1002/qj.49709540607

GOES-R. (2020b). Algorithm theoretical basis document for daytime cloud optical and microphysical properties (DCOMP), Version 1.2. Retrieved from https://www.star.nesdis.noaa.gov/goesr/documents/ATBDs/Enterprise/ATBD_Enterprise_Daytime_Cloud_Optical_and_Microphysical_Properties(DCOMP)_v1.2_2020-10-09.pdf

GOES R. (2020a). Enterprise algorithm working group (AWG) cloud height algorithm (ACHA), Version 3.4. Retrieved from https://www.star.nesdis.noaa.gov/goesr/documents/ATBDs/Enterprise/ATBD_Enterprise_Cloud_Height_v3.4_2020-09.pdf

Goessling, H. F., Rackow, T., & Jung, T. (2025). Recent global temperature surge intensified by record-low planetary albedo. *Science*, *387*(6729), 68–73. https://doi.org/10.1126/science.adq7280

Hess, M., Koepke, P., & Schult, I. (1998). Optical properties of aerosols and clouds: The software package OPAC. *Bulletin of the American Meteorological Society*, *79*(5), 831–844. https://doi.org/10.1175/1520-0477(1998)079<0831:OPOAAC>2.0.CO;2

Horváth, Á., Vadas, S. L., Stephan, C. C., & Buehler, S. A. (2024). One-minute resolution GOES-R observations of Lamb and gravity waves triggered by the Hunga Tonga-Hunga Ha'apai eruptions on 15 January 2022. *Journal of Geophysical Research: Atmospheres*, *129*(3), e2023JD039329. https://doi.org/10.1029/2023JD039329

Khaykin, S., Podglajen, A., Ploeger, F., Grooß, J.-U., Tence, F., Bekki, S., et al. (2022). Global perturbation of stratospheric water and aerosol burden by Hunga eruption. *Communications Earth & Environment*, *3*(1), 316. https://doi.org/10.1038/s43247-022-00652-x

Koren, I., Remer, L. A., Kaufman, Y. J., Rudich, Y., & Martins, J. V. (2007). On the twilight zone between clouds and aerosols. *Geophysical Research Letters*, *34*(8), L08805. https://doi.org/10.1029/2007GL029253

Kubota, T., Saito, T., & Nishida, K. (2022). Global fast-traveling tsunamis driven by atmospheric Lamb waves on the 2022 Tonga eruption. *Science*, *377*(6601), 91–94. https://doi.org/10.1126/science.abo4364

Matoza, R. S., Fee, D., Assink, J. D., Iezzi, A. M., Green, D. N., Kim, K., et al. (2022). Atmospheric waves and global seismoacoustic observations of the January 2022 Hunga eruption, Tonga. *Science*, *377*(6601), 95–100. https://doi.org/10.1126/science.abo7063

Mieslinger, T., Stevens, B., Kölling, T., Brath, M., Wirth, M., & Buehler, S. A. (2022). Optically thin clouds in the trades. *Atmospheric Chemistry and Physics*, *22*(10), 6879–6898. https://doi.org/10.5194/acp-22-6879-2022

Millán, L., Santee, M. L., Lambert, A., Livesey, N. J., Werner, F., Schwartz, M. J., et al. (2022). The Hunga Tonga-Hunga Ha'apai hydration of the stratosphere. *Geophysical Research Letters*, *49*(13), e2022GL099381. https://doi.org/10.1029/2022GL099381

Otsuka, S. (2022). Visualizing Lamb waves from a volcanic eruption using meteorological satellite Himawari-8. *Geophysical Research Letters*, *49*(8), e2022GL098324. https://doi.org/10.1029/2022GL098324

Pekeris, C. L. (1937). Atmospheric oscillations. *Proceedings of the Royal Society of London*, *A*(158A), 650–671. https://doi.org/10.1098/rspa.1937.0046

Perry, K. D., & Hobbs, P. V. (1996). Influences of isolated cumulus clouds on the humidity of their surroundings. *Journal of the Atmospheric Sciences*, *53*(1), 159–174. https://doi.org/10.1175/1520-0469(1996)053<0159:IOICCO>2.0.CO;2

Prata, F., Prata, A. T., Tanner, R., Grainger, R. G., Borgas, M., & Aubry, T. J. (2025). The radial spreading of volcanic umbrella clouds deduced from satellite measurements. *Volcanica*, *8*(1), 1–29. https://doi.org/10.30909/vol.08.01.0129

Purkis, S. J., Ward, S. N., Fitzpatrick, N. M., Garvin, J. B., Slayback, D., Cronin, S. J., et al. (2023). The 2022 Hunga-Tonga megatsunami: Near-field simulation of a once-in-a-century event. *Science Advances*, *9*(15), eadf5493. https://doi.org/10.1126/sciadv.adf5493

PurpleAir. (2025). PurpleAir. Inc. [Dataset]. Retrieved from https://www2.purpleair.com/

Randel, W. J., Johnston, B. R., Braun, J. J., Sokolovskiy, S., Vömel, H., Podglajen, A., & Legras, B. (2023). Stratospheric water vapor from the Hunga Tonga–Hunga Ha'apai volcanic eruption deduced from COSMIC-2 radio occultation. *Remote Sensing*, *15*(8), 2167. https://doi.org/10.3390/rs15082167

Schmit, T. J., Griffith, P., Gunshor, M. M., Daniels, J. M., Goodman, S. J., & Lebair, W. J. (2017). A closer look at the ABI on the GOES-R Series. *Bulletin of the American Meteorological Society*, *98*(4), 681–698. https://doi.org/10.1175/BAMS-D-15-00230.1

Schmit, T. J., Lindstrom, S. S., Gerth, J. J., & Gunshor, M. M. (2018). Applications of the 16 spectral bands on the Advanced Baseline Imager (ABI). *Journal of Operational Meteorology*, *6*(4), 33–46. https://doi.org/10.15191/nwajom.2018.0604

Sepúlveda, I., Carvajal, M., & Agnew, D. C. (2023). Global winds shape planetary-scale Lamb waves. *Geophysical Research Letters*, *50*(19), e2023GL106097. https://doi.org/10.1029/2023GL106097

Sicard, M., Baron, A., Ranaivombola, M., Gantois, D., Millet, T., Sellitto, P., et al. (2025). Radiative impact of the Hunga stratospheric volcanic plume: Role of aerosols and water vapor over Réunion Island (21°S, 55°E). *Atmospheric Chemistry and Physics*, *25*(1), 367–381. https://doi.org/10.5194/acp-25-367-2025

Stocker, M., Steiner, A. K., Ladstädter, F., Foelsche, U., & Randel, W. J. (2024). Strong persistent cooling of the stratosphere after the Hunga eruption. *Communications Earth & Environment*, *5*, 450. https://doi.org/10.1038/s43247-024-01620-3

Su, W., Schuster, G. L., Loeb, N. G., Rogers, R. R., Ferrare, R. A., Hostetler, C. A., et al. (2008). Aerosol and cloud interaction observed from high spectral resolution lidar data. *Journal of Geophysical Research*, *113*(D24), D24202. https://doi.org/10.1029/2008JD010588

Tackett, J. L., & Di Girolamo, L. (2009). Enhanced aerosol backscatter adjacent to tropical trade wind clouds revealed by satellite-based lidar. *Geophysical Research Letters*, *36*(14), L14804. https://doi.org/10.1029/2009GL039264

Tölle, M. H., & Krueger, S. K. (2014). Effects of entrainment and mixing on droplet size distributions in warm cumulus clouds. *Journal of Advances in Modeling Earth Systems*, *6*(2), 281–299. https://doi.org/10.1002/2012MS000209

Twohy, C. H., Coakley, J. A., Jr., & Tahnk, W. R. (2009). Effect of changes in relative humidity on aerosol scattering near clouds. *Journal of Geophysical Research*, *114*(D5), D05205. https://doi.org/10.1029/2008JD010991

Vadas, S. L., Figueiredo, C., Becker, E., Huba, J. D., Themens, D. R., Hindley, N. P., et al. (2023). Traveling ionospheric disturbances induced by the secondary gravity waves from the Tonga eruption on 15 January 2022: Modeling with MESORAC/HIAMCM/Sami3 and comparison with GPS/TEC and ionosonde data. *Journal of Geophysical Research: Space Physics*, *128*(6), e2023JA031408. https://doi.org/10.1029/2023JA031408

Van Eaton, A. R., Lapierre, J., Behnke, S. A., Vagasky, C., Schultz, C. J., Pavolonis, M., et al. (2023). Lightning rings and gravity waves: Insights into the giant eruption plume from Tonga's Hunga Volcano on 15 January 2022. *Geophysical Research Letters*, *50*(12), e2022GL102341. https://doi.org/10.1029/2022GL102341

Várnai, T., & Marshak, A. (2009). MODIS observations of enhanced clear sky reflectance near clouds. *Geophysical Research Letters*, *36*(6), L06807. https://doi.org/10.1029/2008GL037089

Várnai, T., & Marshak, A. (2011). Global CALIPSO observations of aerosol changes near clouds. *IEEE Geoscience and Remote Sensing Letters*, *8*(1), 19–23. https://doi.org/10.1109/LGRS.2010.2049982

Vergoz, J., Hupe, P., Listowski, C., Le Pichon, A., Garcés, M. A., Marchetti, E., et al. (2022). IMS observations of infrasound and acoustic-gravity waves produced by the January 2022 volcanic eruption of Hunga, Tonga: A global analysis. *Earth and Planetary Science Letters*, *591*, 117639. https://doi.org/10.1016/j.epsl.2022.117639

Vicari, R., Stephan, C. C., Lane, T. P., & Huang, Y. (2024). Analysis of trapped small-scale internal gravity waves automatically detected in satellite imagery. *Journal of Geophysical Research: Atmospheres*, *129*(4), e2023JD038956. https://doi.org/10.1029/2023JD038956

Wang, Y., & Huang, Y. (2024). Compensating atmospheric adjustments reduce the volcanic forcing from Hunga stratospheric water vapor enhancement. *Science Advances*, *10*(32), eadl2842. https://doi.org/10.1126/sciadv.adl2842

Watada, S., Imanishi, Y., & Tanaka, K. (2023). Detection of air temperature and wind changes synchronized with the Lamb wave from the 2022 Tonga volcanic eruption. *Geophysical Research Letters*, *50*(2), e2022GL100884. https://doi.org/10.1029/2022GL100884

Watanabe, S., Hamilton, K., Sakazaki, T., & Nakano, M. (2022). First detection of the Pekeris internal global atmospheric resonance: Evidence from the 2022 Tonga eruption and from global reanalysis data. *Journal of the Atmospheric Sciences*, *79*(11), 3027–3043. https://doi.org/10.1175/JAS-D-22-0078.1

Wright, C. J., Hindley, N. P., Alexander, M. J., Barlow, M., Hoffmann, L., Mitchell, C. N., et al. (2022). Surface-to-space atmospheric waves from Hunga Tonga–Hunga Ha'apai eruption. *Nature*, *609*(7928), 741–746. https://doi.org/10.1038/s41586-022-05012-5

Zhou, X., Painemal, D., Gettleman, A., & Feingold, G. (2025). Exploring causal relationships and adjustment timescales of aerosol-cloud interactions in geostationary satellite observations and CAM6 using wavelet phase coherence analysis. *Geophysical Research Letters*, *52*(2), e2024GL111961. https://doi.org/10.1029/2024GL111961

References From the Supporting Information

Bolton, D. (1980). The computation of equivalent potential temperature. *Monthly Weather Review*, *108*(7), 1046–1053. https://doi.org/10.1175/1520-0493(1980)108<1046:TCOEPT>2.0.CO;2